New Design Concept of a Bidirectional Wireless Power Transfer System using Dual Active Bridge Topology

Ha Pham N.
University of Technology, Sydney
Email: phamngocha@ieee.org

***Abstract*—This paper proposes a new design concept of small air-gap bidirectional Wireless Power Transfer (WPT) system using Dual Active Bridge (DAB) topology. The wireless charging coils are considered as a weakly coupled transformer having relatively high leakage inductance, and thus the new design can obtain soft switching without implementing resonant capacitor or external inductor. This design has a simple construction and can enable bidirectional inductive power transfer with superior performance compared to the traditional large air-gap system. The new system can transfer high power via a compact coil structure thanks to smaller air gap. Moreover, soft-switching operation enables significant improvement in efficiency. The proposed design enables electrical vehicles and smart wheels to use batteries for supporting grid silently and seamlessly. This paper considers the application of smart wheel charger and presents an analytical design of the system using finite element analysis and circuit simulation. As a result, the design can achieve 97% efficiency at 3-kW, 85-kHz operation.**

***Index Terms*—wireless power transfer, small air gap, soft switching, finite element analysis.**

I. Introduction

Some countries have already made plans to move toward electrical vehicles (EVs) as the transportation of the future. However, grid support using vehicle batteries is not well developed. Statistically, 95% of cars are parked at any given time, and hence the batteries in EVs could act as a buffer to support the grid. Early attempts to exchange electricity between vehicle batteries and the grid still need fundamental improvements in terms of efficiency and cost. In the future generation of EVs, vehicle-to-grid (V2G) technology is showing great promise as a way to fully utilise vehicle batteries as a way to bolster grid capacity and save cost [1]–[3].

At the moment, EV chargers rely on plug-in connectors, which are bulky and inconvenient for the users. Moreover, their high-power charging requirements significantly increase the risk of electrocution, especially in rain or humid weather. Moreover, adverse environment such as snow or ice can freeze the chargers and make it difficult to access. Wireless Power Transfer (WPT), or Inductive Power Transfer (IPT), has been developed as a solution to these problems to charge batteries without contact and thus free of maintenance. Most existing products are uni-directional and only support grid-to-vehicle (G2V) charging [4], [5].

Of a few bi-directional inductive power transfer schemes that have been proposed [6], [7], efficiency remains low. Soft switching is difficult to achieve and thus, the switching frequency stays well below the standard 85 kHz required by the automotive industry [8].

Existing WPT products on the market consider charger placed at the bottom of vehicles, leading to large air-gap and thus the system has efficiency limitation and safety concerns. There are a few alternate solutions such as robotic arm contact charger [9] or movable contact-less charger [10]. However, the moving parts are not as attractive as the original WPT design where maintenance is not required.

This paper suggests that the moving parts can be eliminated if the car is equipped with automated parking [11], [12]. In such case, the air gap between transmitter and receiver coils can be much smaller and hence, a new WPT design should be considered. This type of design is particular applicable for existing smart wheel concepts such as Copenhagen Wheel, FlyKly, Daymak DDS and GeoOrbital.

At small air gap, the WPT coil system could be considered as a weakly coupled transformer having a movable air gap between the primary and secondary coils. This structure enables an improved coupling factor as well as a reasonable leakage inductance, which are applicable to Dual Active Bridge (DAB) [13]–[17]. The DAB topology is well known for very high efficiency with optimization [18], advanced modulation [19], and SiC device implementation [20]. This paper proposes a simple WPT design that enables soft switching without additional inductor or resonant capacitor, thus the WPT system is simple to implement and can operate at low power loss. The system can enhance battery utilization significantly thanks to its superior efficiency and the capability of bidirectional power control.

This paper applies finite element analysis (FEA) to design a suitable inductive coil system and models it as a high-leakage transformer. A theoretical formula is developed to model the power transfer according to the self-inductances and coupling factor of the WPT coils. Circuit simulation is used to study the performance of the proposed WPT system. As a result, it is confirmed that the WPT system can maintain soft switching under various conditions and obtain a power transfer efficiency as high as 97%.

II. Design Concept and Circuit Diagram

Fig. 1 illustrates a design concept of the proposed WPT system which is applicable to smart wheel concept such as the Copenhagen wheel. The transmitter consisting of a primary winding is placed on a charging station installed near

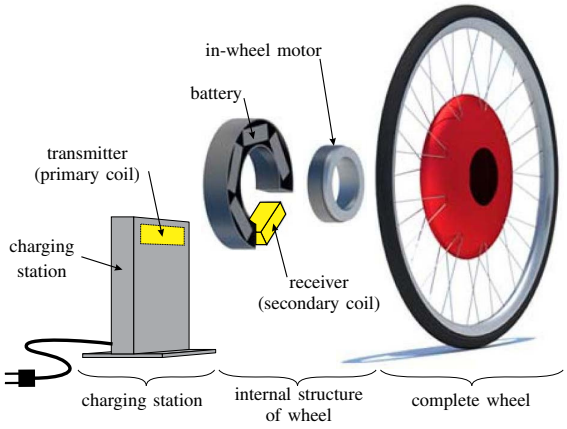

Fig. 1. Design concept for smart wheel charger (e.g. in Copenhagen wheel).

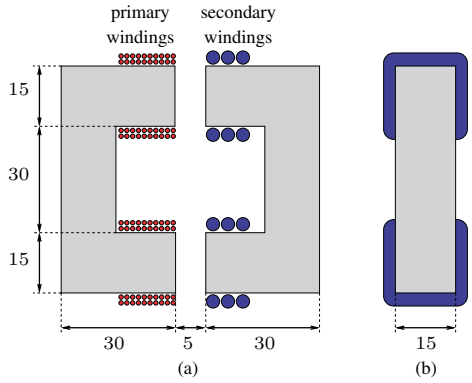

Fig. 2. Cross sections of the WPT coil system wound on double U cores: (a) front view, and (b) side view. Unit: mm.

the parking position. The receiver with a secondary winding connected to a battery is positioned in the smart wheel and can be adjusted to be near the position of the transmitter. The WPT system connects the battery on the wheel to the grid, which is represented by a 400-V dc link.

Fig. 2 shows the dimension of the WPT coil system at the optimal position. The air-gap represents the housings outside the transmitter and receiver. The minimal air-gap is assumed to be 5 mm considering the housing of the device. However, this gap may be increased due to displacement or misalignment. This paper analyses the WPT system under possible misalignment Δx and Δy in horizontal and vertical directions using 2-D FEA. The windings are situated on symmetrical double U Ferrite cores. The size of core was chosen so that it can transmit 3-kW power at 85 kHz without saturation.

The circuit diagram of the WPT system is shown in Fig. 3. It has a simple construction with two full bridges (DAB) connected with each other via the coupling coils. Since the topology has non-negligible dc current ripples at the input and output, low ESR capacitors C_1 and C_2 are employed as filter. The filter capacitors are chosen based on their rated ripple currents. The circuit parameters are given in Table I. Litz wire with AWG38 strands is used to form the windings and reduce skin and proximity effects at 85 kHz. The primary winding

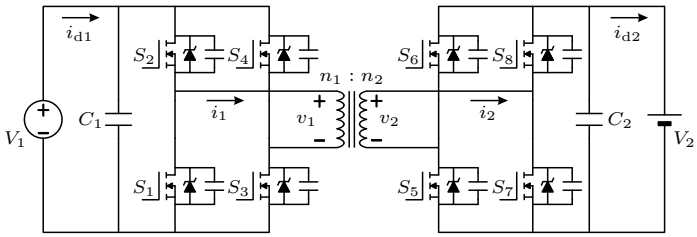

Fig. 3. Circuit configuration of the WPT system.

TABLE I
CIRCUIT PARAMETERS.

switching frequency	f_{sw}	85 kHz
input voltage	V_1	400 V
battery voltage	V_2	60 V
input bridge	S_1–S_4	IXFB150N65X2
output bridge	S_5–S_8	IPT015N10N5ATMA1
input filter capacitor	C_1	B32754C2106K000
output filter capacitor	C_2	PCR1J101MCL1GS×20
Ferrite core	U shape	N97 material
primary coil	AWG38×100 strands	1.3-mm diameter
secondary coil	AWG38×1000 strands	4.3-mm diameter
primary windings	n_1	40
secondary windings	n_2	6

has two layers of 10 turns on each leg, while the secondary winding has a single layer of 3 turns on each leg.

III. Circuit Analysis

The theoretical analysis of DAB operation in case of strong coupling was considered in [13], where the leakage inductances referred to the primary side of the two coils are considered to be similar, i.e. $L_1 = L_2'$. However, this assumption is not necessarily true in all the cases. This paper reveals a more general derivation considering a relatively weaker coupling coil system that can be used in WPT.

Fig. 4 shows an equivalent circuit referred to the primary side of the WPT coil system where the loss is neglected. L_1, L_2' are the leakage inductances in the primary and secondary coils respectively, and $L_{\rm m}$ is their mutual (or magnetizing) inductance.

A simple circuit analysis applied to Fig. 4 yields

$$\frac{di_1}{dt} = \frac{v_1}{l_1} - \frac{v_2'}{l_2} \quad (1)$$

$$\frac{di_2'}{dt} = \frac{v_1}{l_2} - \frac{v_2'}{l_1}, \quad (2)$$

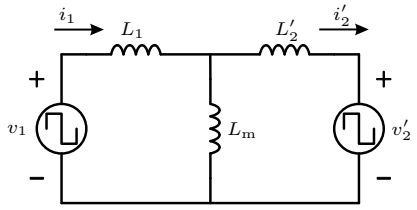

Fig. 4. Equivalent circuit of the WPT coil system.

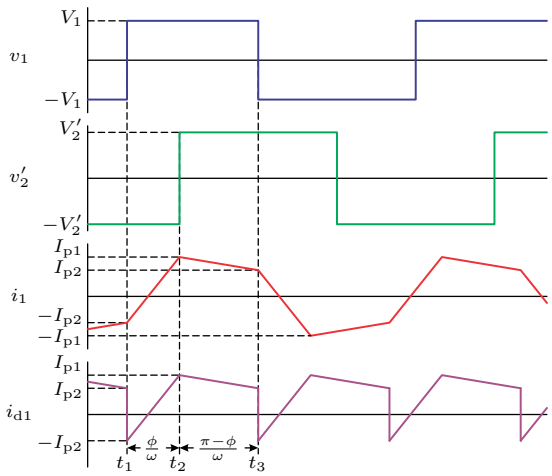

Fig. 5. Theoretical waveforms of the DAB in steady state.

where the equivalent inductances l_1 and l_2 are given by

$$l_1 = L_1 + \frac{L_2' L_m}{L_2' + L_m} \quad (3)$$

$$l_2 = L_1 + L_2' + \frac{L_1 L_2'}{L_m}. \quad (4)$$

Considering the case when the phase-shift ϕ takes positive value, the steady state waveforms of the DAB can be explained by Fig. 5. The full bridge outputs v_1 and v_2 are two-level waveforms at 100% duty cycle, with a phase-shift angle ϕ. During switching periods (t_1, t_2) and (t_2, t_3), the change in primary current i_1 from (1) becomes

$$(t_1, t_2) \; : \; \omega \frac{I_{p1} + I_{p2}}{\phi} = \frac{V_1}{l_1} + \frac{V_2'}{l_2} \quad (5)$$

$$(t_2, t_3) \; : \; \omega \frac{I_{p1} - I_{p2}}{\pi - \phi} = \frac{V_1}{l_1} - \frac{V_2'}{l_2}. \quad (6)$$

Solving (5)–(6) yields the shape of input current. The switching of the primary side occurs at $t = t_1$ and $t = t_3$ when:

$$I_{sw1} = I_{p2} = \left(\phi - \frac{\pi}{2}\right) \frac{V_1}{\omega l_1} + \frac{\pi}{2} \frac{V_2'}{\omega l_2}. \quad (7)$$

Soft switching happens at the input bridge when $I_{sw1} > 0$, thus from (7) we have

$$\frac{V_2'}{V_1} > \frac{l_1}{l_2} \left(1 - \frac{2\phi}{\pi}\right). \quad (8)$$

Similar calculation at the secondary side yields the switching current at the output bridge as

$$I_{sw2} = n \left[\frac{\pi}{2} \frac{V_1}{\omega l_2} + \left(\phi - \frac{\pi}{2}\right) \frac{V_2'}{\omega l_1}\right], \quad (9)$$

where $n = n_1/n_2$ is the turn ratio of the WPT coil system. Hence its corresponding soft switching condition is

$$\frac{V_2'}{V_1} < \frac{l_2}{l_1} \frac{\pi}{\pi - 2\phi}. \quad (10)$$

On the other hand, the average input current at the primary side is given by

$$I_{d1} = \int_{t_1}^{t_3} i_{d1} dt = \frac{V_2'}{\omega l_2} \phi \left(1 - \frac{\phi}{\pi}\right). \quad (11)$$

Calculate the input power to the DAB by multiplying the input voltage with (11), we obtain

$$P = V_1 I_{d1} = \frac{V_1 V_2'}{\omega l_2} \phi \left(1 - \frac{\phi}{\pi}\right). \quad (12)$$

Applying the same calculation for the case of negative ϕ, it can be concluded that for the general case, the power transferred by the DAB is

$$P = \frac{V_1 V_2'}{\omega l_2} \phi \left(1 - \frac{|\phi|}{\pi}\right). \quad (13)$$

The results agree with [13], however under weaker coupling condition, l_2 depends on the mutual inductance L_m, and thus is higher than the total leakage inductance according to (4).

In general, the WPT coil system can be modelled by the self inductances of the primary coil L_{11}, the secondary coil L_{22} (or L_{22}' as referred to the primary side) and their coupling factor K as follows

$$L_m = K\sqrt{L_{11} L_{22}'} \quad (14)$$

$$L_{11} = L_1 + L_m \quad (15)$$

$$L_{22}' = L_2' + L_m. \quad (16)$$

Subtituting the self inductances and the coupling factor to (13), we obtain

$$P = \frac{K}{1 - K^2} \frac{V_1 V_2'}{\omega \sqrt{L_{11} L_{22}'}} \phi \left(1 - \frac{|\phi|}{\pi}\right). \quad (17)$$

On the other hand, the soft-switching boundaries for the primary and secondary sides from (8) and (10) become

$$\beta < \frac{V_2'}{V_1} < \frac{1}{\beta} \quad (18)$$

where

$$\beta = K\sqrt{\frac{L_{11}}{L_{22}'}} \left(1 - \frac{2\phi}{\pi}\right). \quad (19)$$

IV. Design and Control Methodology

As the WPT system needs to deal with uncertainty in the charging/discharging position, FEA software FEMM was used for analyzing the self-inductances of the WPT coils and their coupling factor in various positions. As can be seen from Figs. 6(a) and (b), all circuit parameters decline under misalignment. However, the horizontal misalignment Δx has much less effect than the vertical one Δy. The reason for this difference is that the magnetic field in the double U cores can leak from the upper leg to the lower leg. The amount of leakage field increases sharply with the vertical misalignment position especially when the upper leg of the primary core approaches the secondary lower leg. It is also noted that there is a slight difference in the self-inductances of coil 1 L_{11} and

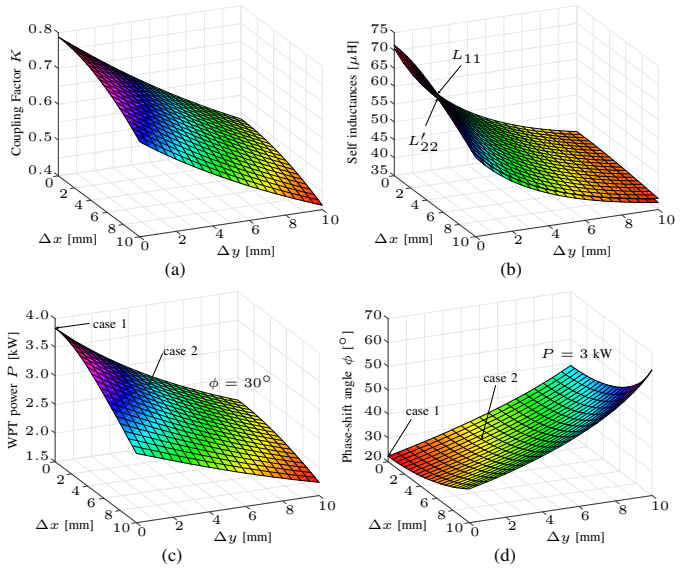

Fig. 6. FEA analysis of the WPT system for various misalignment: (a) coupling factor K, (b) self inductances L_{11} and L'_{22}, (c) power transfer at $\phi = 30°$, and (c) phase-shift angle required to transfer 3-kW power.

TABLE II
OPERATING CONDITIONS.

case 1		
coupling factor	K	0.788
self inductance (primary)	L_{11}	71.5 μH
self inductance (secondary)	L'_{22}	70.5 μH

case 2		
coupling factor	K	0.679
self inductance (primary)	L_{11}	54.0 μH
self inductance (secondary)	L'_{22}	53.0 μH

coil 2 L'_{22} referred to the primary side. The similarity comes from the symmetrical layout of the U cores, while the slight mismatch is from the different size and shape of the windings.

The performance of DAB is usually designed for the case of $\phi = 30°$ due to efficiency consideration. The power calculation according to (17) is illustrated in Fig. 6(c). It can be seen that for a fixed phase-shift angle, there is large variation in power transferred due to misalignment. The best condition for transferring power occurs when there is no mismatch between the two coils, i.e. $\Delta x = \Delta y = 0$ or "case 1". Given the consideration of 3-kW system, the worst case misalignment is considered as "case 2" where only 3-kW power can be transferred. An example of "case 2" was chosen as $\Delta x = 2.5$ mm and $\Delta y = 4$ mm from Fig. 6(c). The detailed parameters for those cases are displayed in Table II and will be then used for circuit simulation to analyse the performance of the DAB circuit.

The theoretical phase-shift value $0 < \phi < \pi/2$ can be extracted from (17) as follows:

$$\phi = \frac{\pi}{2} - \frac{\pi}{2}\sqrt{1 - \frac{P}{P_{\max}}}, \tag{20}$$

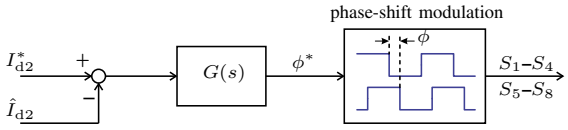

Fig. 7. Battery current control scheme for output bridge.

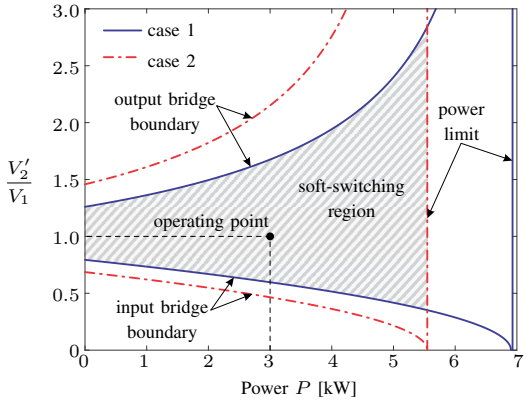

Fig. 8. Operating boundaries of the WPT system.

where

$$P_{\max} = \frac{\pi}{4}\frac{K}{1-K^2}\frac{V_1 V'_2}{\omega\sqrt{L_{11}L'_{22}}} \tag{21}$$

is the maximum power occurred at $\phi = \pi/2$. Because the battery power needs to be controlled to a certain level, it is assumed that the power is fixed at $P = 3$ kW. Fig. 6(d) shows the theoretical value of ϕ needed to obtain a constant 3-kW power using (20). It can be seen that the phase-shift angle need to be varied from 20 to 30° to maintain a stable power transfer for any case between case 1 and case 2.

The power transferred by DAB $P = V_2 I_{d2}$ is controlled by means of controlling the average battery current I_{d2} at the output bridge. A simple current control block for the output bridge of the DAB inverter is explained in Fig. 7. A controller $G(s)$ adjusts the battery current to meet its reference I^*_{d2} via the phase-shift angle ϕ between the voltages of the output and input bridges according to (20). A phase-shift modulation block determines the PWM signals to S_1–S_8.

Fig. 8 shows the theoretical operating boundaries of the DAB in the WPT system. The input and output limits of the DAB are given by (18), while the power limit is given by (21) when the phase-shift angle reaches $\phi = \pi/2$. The soft-switching operation of the DAB is possible in the overlapping area created by the boundary lines of the two cases. It can be seen that the soft switching operation is warranted at the current operating point where $P = 3$ kW and $V'_2 = V_1$. According to Fig. 8, the soft-switching can be further obtained for a wide range of input and output voltages, which means the battery voltage can vary under different state of charge (SoC) while the input capacitor can be designed to be small to save cost. The worst scenarios occurs at $P = 0$ (or $\phi = 0$) in case 1 where the coupling factor is highest and hence, all design constrains for soft switching must be considered here.

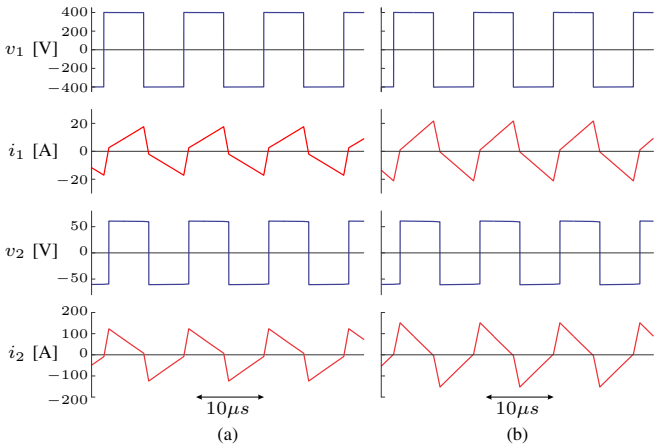

Fig. 9. Simulated waveforms of the WPT system at 3 kW, 85 kHz for: (a) case 1, and (b) case 2.

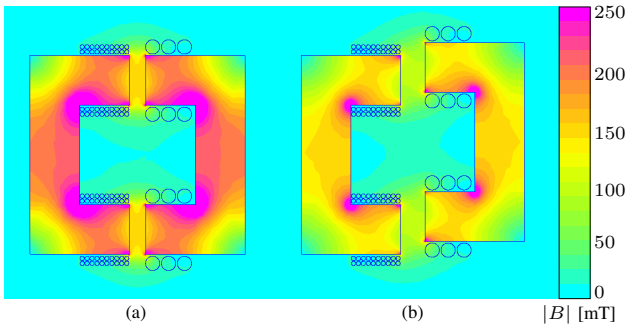

Fig. 10. 2D FEM simulation results for transfering 3-kW power to charge the battery in: (a) case 1 at minimal air gap, and (b) case 2 where there is a misalignment.

V. Simulation Results

Simulation was carried out to evaluate the operations of the WPT system. First, circuit simulation was applied to get the operating waveforms in the circuitry. The results were later used to estimate the conduction and switching losses in the switching devices. FEA simulation was again carried out to study the copper loss and core loss in the WPT coil system.

A. Steady-state operation

Figs. 9(a) and (b) show the voltage and current waveforms of the WPT coils operating at 3 kW, 85 kHz for cases 1 and 2. The phase-shift angle ϕ is increased by the controller to maintain the power and adapt to the changing in charging position. At the higher phase-shift angle, the currents have a higher peak values which are also the turn-off currents at the input and output bridges.

Although the input and output voltages referred to the primary side are equal, it can be seen that the current waveforms are different compared to those in a typical DAB circuitry where they should take similar shapes. This implies that the input and output currents contain a non-negligible magnetizing current and thus increase the turn-off currents. Higher magnetizing current can ensure soft switching, however the efficiency is compromised due to extra conduction and switching losses.

B. Loss analysis

It is assumed that losses in the WPT system consists of three types of losses: Ohmic loss, switching loss, and core loss [20].

1) Ohmic loss: This paper considers three types of Ohmic losses in: filter capacitor $P_{\text{cap.}}$, MOSFET conduction $P_{\text{cond.}}$ and copper in the coil windings P_{Cu}. From the simulated waveforms, the Ohmic loss in each part can be extracted from:

$$P_{\text{cap.}} = I_{\text{rms}}^2 ESR, \tag{22}$$

$$P_{\text{cond.}} = I_{\text{rms}}^2 R_{\text{ds(on)}}, \tag{23}$$

$$P_{\text{Cu}} = I_{\text{rms}}^2 R_{\text{winding}}, \tag{24}$$

where I_{rms} is the rms current flowing through the part under consideration, ESR is the equivalent series resistance of the capactitor given by the datasheet, $R_{\text{ds(on)}}$ is assumed to be the worst case resistance at junction temperature of $T_{\text{j}} = 100°$, and R_{winding} is the winding resistance measured at each terminal. Notice that the interaction of the two coils is not considered in this simple loss estimation.

2) Switching loss: The switching loss in each switching device can be considered to be proportional to the square of switching current as suggested in [20] as follows:

$$P_{\text{sw}} = E_{\text{sw}} f_{\text{sw}} = \frac{T_{\text{f}}}{48C} I_{\text{sw}}^2 f_{\text{sw}}, \tag{25}$$

where T_{f} is a transient time constant, C is an equivalent drain to source capacitance including external snubber capacitance, and I_{sw} is the swithching current given by (7) and (9). In this paper, for the sake of quick estimation, it is assumed that $T_{\text{f}} = 100$ ns, $C = 2.2$ nF and 47 nF at the input and output bridges, respectively.

3) Core loss: The core loss in Ferrite is estimated via magnetic flux density B generated by FEA. The operating currents shown in Figs. 9(a) and (b) are extracted to the FEA program and used to produce the flux density map. The flux density is then used to estimate the core loss via an approximated Steinmetz equation extracted from the datasheet of Ferrite N97.

Figs. 10(a) and (b) illustrate the flux density map according operation at 3 kW, 85 kHz of the cases 1 and 2, respectively. It can be seen that the flux density is reduced when the air gap increased. This is because the same amount of transfered energy is stored in an increased volume air gap.

C. Estimated performance

1) Loss breakdown: Fig. 11 shows the estimated losses in the WPT system for the two cases at 3-kW, 85-kHz operation. It can be seen that the conduction and switching losses at full bridges are dominant due to the low voltage devices. The filter capacitor loss is negligible at the high voltage side due to small current, but at the low voltage side it is considerably large. On the other hand the losses in the coil system is quite small and is dominated by core loss. Therefore, the system

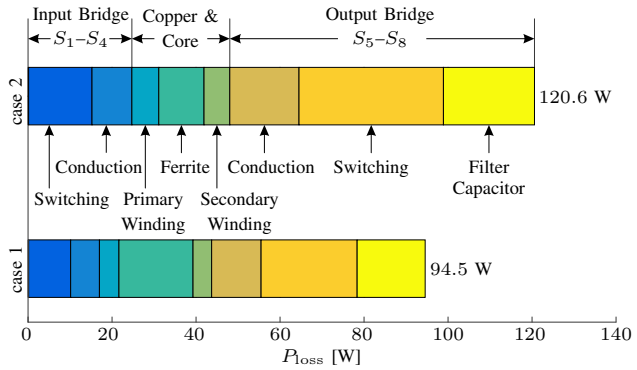

Fig. 11. Power loss breakdown at 3-kW, 85-kHz operation for the two cases.

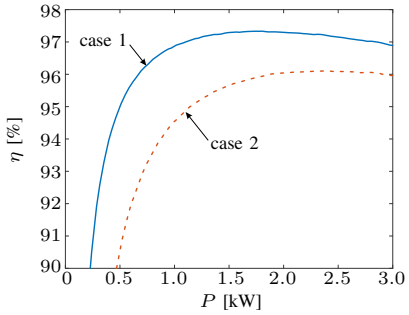

Fig. 12. Calculated efficiency of the WPT system according to the loss estimation.

can be further improved by paralleling switching devices and increase the filter capacitor at the secondary side.

As shown in Figs. 10, the core loss in case 1 is more than that in case 2 because of the small air gap. However, due to higher excitation current required, the other losses increase and thus the total loss becomes 120.6 W compared to only 94.5 W in case of small air gap.

2) Efficiency evaluation: Fig. 12 shows the calculated efficiency of the WPT system based on the loss estimation for various operating points. The system is best used when the gap is minimal as in case 1. Larger air gap such as case 2 will lead to significant drop in efficiency. Also, the performance drops quickly at low power due to high magnetizing current.

The relatively weak coupling factor in the WPT coils which requires high magnetizing current and causes higher conduction and switching losses compared to that in a typical DAB circuitry. Nevertheless, the estimated efficiency is still much higher than that in large air-gap WPT systems.

VI. Conclusion

This paper proposed a new design for bidirectional WPT system applicable to electrical vehicles in general and smart wheels in particular. The new design employs a DAB circuitry with two bridges operating under phase-shift modulation. It only requires a compact coil system and can achieve soft-switching performance. This paper reveals theoretical analysis of the WPT system, showing how the DAB circuit works under relatively weak coupling condition. Simulation based study showed that the proposed design is capable of transferring 3-kW, 85-kHz power at efficiency as high as 97%.

References

[1] P. H. Kydd, J. R. Anstrom, P. D. Heitmann, K. J. Komara and M. E. Crouse, "Vehicle-Solar-Grid Integration: Concept and Construction," *IEEE Power and Energy Tech. Sys. Journal,* vol. 3, no. 3, pp. 81–88, Sept. 2016.

[2] M. C. Kisacikoglu, M. Kesler and L. M. Tolbert, "Single-Phase On-Board Bidirectional PEV Charger for V2G Reactive Power Operation," *IEEE Trans. Smart Grid,* vol. 6, no. 2, pp. 767-775, March 2015.

[3] M. J. E. Alam, K. M. Muttaqi and D. Sutanto, "Effective Utilization of Available PEV Battery Capacity for Mitigation of Solar PV Impact and Grid Support With Integrated V2G Functionality," *IEEE Trans. Smart Grid,* vol. 7, no. 3, pp. 1562-1571, May 2016.

[4] John M. Miller; Andrew Daga, "Elements of Wireless Power Transfer Essential to High Power Charging of Heavy Duty Vehicles," *IEEE Trans. Transportation Electrification,* vol. 1 no. 1, pp. 26–39, 2015.

[5] S. Zhou and C. Chris Mi, "Multi-Paralleled LCC Reactive Power Compensation Networks and Their Tuning Method for Electric Vehicle Dynamic Wireless Charging," *IEEE Trans. Ind. Electron.,* vol. 63, no. 10, pp. 6546-6556, Oct. 2016.

[6] U. K. Madawala and D. J. Thrimawithana, "A Bidirectional Inductive Power Interface for Electric Vehicles in V2G Systems," *IEEE Trans. Ind. Electron.,* vol. 58, no. 10, pp. 4789–4796, Oct. 2011.

[7] A. K. Swain, S. Devarakonda and U. K. Madawala, "Modeling, Sensitivity Analysis, and Controller Synthesis of Multipickup Bidirectional Inductive Power Transfer Systems," *IEEE Trans. Ind. Informatics,* vol. 10, no. 2, pp. 1372–1380, May 2014.

[8] SAE International, "SAE TIR J2954 Wireless Power Transfer for Light-Duty Plug-In/ Electric Vehicles and Alignment Methodology," *Standard,* May 17, 2016.

[9] J. Mardall and C. H. Van Dyke, "Charging station providing thermal conditioning of electric vehicle during charging session," *Patent,* publication no. US20170096073 A1, Apr 6, 2017.

[10] Ha Pham N., "Movable Magnetic Core Wireless Chargers Applicable for Electrical Vehicles," *Patent,* publication no. WO 2015067816 A1, May 14, 2015.

[11] D. Gorinevsky, A. Kapitanovsky and A. Goldenberg, "Neural network architecture for trajectory generation and control of automated car parking," *IEEE Trans. Control Sys. Tech.,* vol. 4, no. 1, pp. 50–56, Jan 1996.

[12] X. Du and K. K. Tan, "Autonomous Reverse Parking System Based on Robust Path Generation and Improved Sliding Mode Control," *IEEE Transactions on Intelligent Transportation Systems,* vol. 16, no. 3, pp. 1225–1237, June 2015.

[13] R. W. De Doncker, D. M. Divan, and M. H. Kheraluwala, "A three-phase soft-switched high-power-density dc/dc converter for high power applications," *IEEE Trans. Ind. Appl.,* vol. 27, no. 1, pp. 63–73, Jan./Feb. 1991.

[14] M. H. Kheraluwala, R. W. Gascoigne, D. M. Divan, and E. D. Baumann, "Performance characterization of a high-power dual active bridge dc-todc converter," *IEEE Trans. Ind. Appl.,* vol. 28, no. 6, pp. 1294–1301, Nov./Dec. 1992.

[15] R. L. Steigerwald, R. W. De Doncker, and M. H. Kheraluwala, "A comparison of high-power dcdc soft-switched converter topologies," *IEEE Trans. Ind. Appl.,* vol. 32, no. 5, pp. 1139–1145, Sep./Oct. 1996.

[16] X. Li and A. K. S. Bhat, "Analysis and Design of High-Frequency Isolated Dual-Bridge Series Resonant DC/DC Converter," *IEEE Trans. Power Electron.,* vol. 25, no. 4, pp. 850–862, April 2010.

[17] P. Xuewei and A. K. Rathore, "Novel Bidirectional Snubberless Naturally Commutated Soft-Switching Current-Fed Full-Bridge Isolated DC/DC Converter for Fuel Cell Vehicles," *IEEE Trans. Ind. Electron.,* vol. 61, no. 5, pp. 2307–2315, May 2014.

[18] F. Krismer and J. W. Kolar, "Efficiency-Optimized High-Current Dual Active Bridge Converter for Automotive Applications," *IEEE Trans. Power Electron.,* vol. 59, no. 7, pp. 2745–2760, July 2012.

[19] J. Everts, F. Krismer, J. Van den Keybus, J. Driesen and J. W. Kolar, "Optimal ZVS Modulation of Single-Phase Single-Stage Bidirectional DAB ACDC Converters," *IEEE Trans. Power Electron.,* vol. 29, no. 8, pp. 3954–3970, Aug. 2014.

[20] H. Akagi, T. Yamagishi, N. M. L. Tan, S. i. Kinouchi, Y. Miyazaki and M. Koyama, "Power-Loss Breakdown of a 750-V 100-kW 20-kHz Bidirectional Isolated DCDC Converter Using SiC-MOSFET/SBD Dual Modules," *IEEE Trans. Ind. Appl.,* vol. 51, no. 1, pp. 420–428, Jan.-Feb. 2015.